Electronic Supplementary Material (ESI) for New Journal of Chemistry.
This journal is © The Royal Society of Chemistry and the Centre National de la Recherche Scientifique 2021

Visible-light-driven H_2 production from heterostructured $Zn_{0.5}Cd_{0.5}S$–TiO_2 photocatalysts modified with reduced graphene oxides†

Author and affiliation details can be edited in the panel that appears to the right when you click on the author list.

Na Qin[a,b], Aojie Mao[a], Junhua Zou[b], Liwei Mi,(0000-0001-9239-6599)[a,*] and Ling Wu,(0000-0003-2652-8105)[b,*]

[a]Center for Advanced Materials Research, Zhongyuan University of Technology, Zhengzhou 451191, Henan, China, mlwzzu@163.com

[b]State Key Laboratory of Photocatalysis on Energy and Environment, Fuzhou University, Fuzhou 350002, Fujian, China, wuling@fzu.edu.cn

Funding Information

We have combined the funding information you gave us on submission with the information in your acknowledgements. This will help ensure the funding information is as complete as possible and matches funders listed in the Crossref Funder Registry.

Please check that the funder names and award numbers are correct. For more information on acknowledging funders, visit our website: http://www.rsc.org/journals-books-databases/journal-authors-reviewers/author-responsibilities/#funding.

Funder Name :	National Natural Science Foundation of China
Funder's main country of origin :	
Funder ID :	10.13039/501100001809
Award/grant Number :	21273036
	21872032

Table of Contents Entry

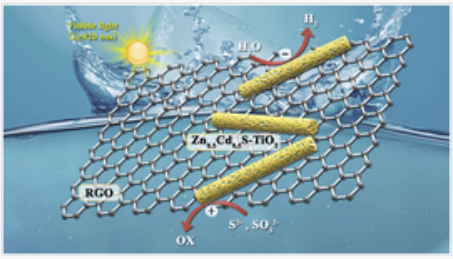

Benefiting from the heterojunction structure and compositional features, the optimized 0.5%RGO/50%$Zn_{0.5}Cd_{0.5}S$–TiO_2 composites exhibited considerable photocatalytic activities for H_2 evolution.

Abstract

Although, hydrogen is a promising green energy source, current catalysts for hydrogen production cannot use the full range of visible light. In addition, these catalysts suffer from problems such as rapid charge-carrier recombination. Therefore, a simple strategy to synthesize high-performance catalysts for visible-light-driven H_2 production is required. One promising method of increasing catalyst efficiency is the use of a heterojunction structure. Therefore, in this study,

$Zn_{0.5}Cd_{0.5}S$–TiO_2 (ZCS–TiO_2) heterojunction photocatalysts were prepared *via* the controlled growth of $Zn_{0.5}Cd_{0.5}S$ using a facile solvothermal method. The ZCS–TiO_2 heterojunction photocatalysts showed high hydrogen production performance from water upon exposure to visible light as a result of the increased separation of photogenerated charges. Based on this success, we further modified the surface of the $Zn_{0.5}Cd_{0.5}S$–TiO_2 catalyst with a reduced graphene oxide (RGO) cocatalyst to produce RGO/ZCS–TiO_2 composite heterojunction photocatalysts. These ternary composite heterojunction photocatalysts also showed good hydrogen production from water because of the enhanced electron transport endowed by RGO and the matching band structure between $Zn_{0.5}Cd_{0.5}S$ and TiO_2. Furthermore, we investigated the effects of different loadings of RGO, as well as the use of physical mixtures, on the catalytic activity; the optimized 0.5%RGO/50%ZCS–TiO_2 composite exhibited distinctly greater photocatalytic activity than the 50%ZCS–TiO_2 and ZCS catalysts, as well as the 0.5%Pt/50%ZCS–TiO_2 catalyst. Thus, our study demonstrates a new approach for obtaining highly efficient ZCS-based photocatalysts.

1. Introduction

Hydrogen (H_2) has attracted much attention as a source of clean energy and an alternative to fossil fuels. However, to be a truly green replacement for fossil fuels, the production of H_2 from renewable resources is necessary. The photocatalytic splitting of water with solar energy is a promising method in this regard because of its low cost and environmental friendliness. To date, many sulfide-based semiconductor materials for photocatalytic H_2 production have been reported because of their suitable band edge positions and narrow band gaps for visible light absorption.[1–5] For example, $Zn_xCd_{1-x}S$ is regarded as an efficient photocatalyst for H_2 production because of its controllable bandgap width and band-edge position.[6–8] However, its photocatalytic H_2 production performance is insufficient for practical applications because of the large particle size, which results in a low number of active sites, as well as the rapid recombination of photogenerated electrons and holes. Therefore, a range of methods such as doping, semiconductor coupling, and cocatalyst loading have been used to improve the catalytic performance of $Zn_xCd_{1-x}S$ for H_2 production.[9–12] In particular, to promote the separation of photogenerated charges, obtain a large number of surface active sites, efficiently utilize visible light, and enhance the photocatalytic H_2 production performance of $Zn_xCd_{1-x}S$, the band structure and composition of multifunctional composites should be optimized.

Recently, one-dimensional (1D) TiO_2 nanostructured materials, such as nanofibers, nanotubes, and nanobelts, have been shown to have significant potential in numerous fields.[13–17] Among these 1D TiO_2 nanostructured materials, nanofibers, which are prepared using a simple electrospinning technique, have attracted particular attention. The 1D electrospun TiO_2 nanofibers have a large aspect ratio, high surface area, and significant porosity, making them useful for photocatalytic applications.[18,19] In addition, they can be assembled into secondary nanostructures with high densities without aggregation, promote the mobility and isolation of photogenerated charge carriers, and aid the recycling of photocatalysts.[20] Concerning sulfide-based photocatalysts, electrospun TiO_2 nanofibers are a suitable support for $Zn_xCd_{1-x}S$ because of their matched conduction bands.[21] Recent studies have shown that the construction of heterojunctions is an effective strategy to promote the spatial separation and effective utilization of photoinduced charges, because the photogenerated electrons and holes can be driven in opposite directions under an applied electric field.[22,23] Therefore, in this study, $Zn_{0.5}Cd_{0.5}S$ (ZCS) was supported on electrospun TiO_2 nanofibers for constructing ZCS-based heterogeneous photocatalysts to enhance the photocatalytic water splitting performance of ZCS.

In addition, to increase the number of surface active sites for H_2 production in ZCS on the 1D electrospun TiO_2 nanofibers, surface modification with cocatalysts was exploited.[24] Noble metals have been demonstrated to be effective cocatalysts for the H_2 evolution reaction,[25,26] but their high cost and scarcity limit their extensive applications. In recent years, graphene has emerged as a common non-noble-metal cocatalyst that has been widely used in photocatalysis because of its large specific surface area, high stability, good electron mobility, and modifiable surface structure.[27–29] In fact, graphene semiconductors show excellent performance for photocatalytic H_2 production from water because of their unique two-dimensional structure and good electron conducting ability.[30–33] Therefore, we modified our ZCS–TiO_2 catalyst with graphene to enhance the H_2 production activity. Crucially, the unmodified and reduced graphene oxide (RGO)-modified ZCS–TiO_2 photocatalysts were prepared using a simple solvothermal method.

We found that the introduction of TiO_2 nanofibers greatly reduced the size of the ZCS nanoparticles and firmly anchored the ZCS to the surface of the nanofibers, thus forming a heterojunction; this significantly reduced carrier recombination in the ZCS and thus improved the photocatalytic H_2 production activity. Furthermore, the introduction of RGO not only enhanced photogenerated electron transfer and separation at the interface but also acted as a cocatalyst to improve the photocatalytic performance of ZCS–TiO_2. Therefore, RGO/ZCS–TiO_2 is a promising system for enhanced visible light photocatalytic H_2 production activity and charge separation.

2. Experimental

2.1. Chemicals

All chemicals were purchased from commercial sources and used without further purification. Deionized water was used during all experiments.

2.2. Photocatalyst synthesis

$Zn_{0.5}Cd_{0.5}S$ (ZCS) supported on TiO_2 nanofibers was prepared through a solvothermal process. The TiO_2 nanofibers were firstly prepared according to our previous works.[34] Then, 25 mg TiO_2 nanofibers and $Cd(Ac)_2 \cdot 2H_2O$ and $Zn(Ac)_2 \cdot 2H_2O$ in a molar ratio of 1 were added to 30 mL of mixed solution containing deionized water and ethanol (v : v = 1 : 1) to form solution A. Meanwhile, 10 mmol of thiourea was dissolved into another 30 mL solution containing deionized water and ethanol (v : v = 1 : 1) to form solution B. Next, solution B was dropped into solution A with stirring and ultrasonication. Subsequently, the mixed solution was transferred into a 100 mL autoclave and maintained at 180 °C for 12 h. After cooling, the precipitates were collected and washed with deionized water and ethanol several times and dried at 60 °C overnight. The obtained products are denoted (*X*)ZCS–TiO_2, where (*X*) = 20%, 30%, 50%, and 70%, representing the amounts of ZCS (20–70%) in the as-prepared ZCS–TiO_2 composites. Additionally, pure ZCS was synthesized using the same method but without the addition of TiO_2 nanofibers.

Details of the preparation of graphene oxide (GO) are provided in the (ESI †). The RGO-wrapped ZCS–TiO_2 composites (RGO/ZCS–TiO_2) were prepared as for (50%)ZCS–TiO_2, except that an aqueous dispersion of graphene oxide (GO) was added to solution A. Based on the amount of GO, the obtained composites were denoted (*x*)RGO/(50%)ZCS–TiO_2, where x = 0.25%, 0.5%, and 1.0%. For comparison, 0.5%Pt/50%ZCS–TiO_2 composites were fabricated by a photodeposition method using $H_2PtCl_6 \cdot 6H_2O$ as the Pt source.

If not specified, ZCS–TiO_2 and RGO/ZCS–TiO_2 indicate (50%)ZCS–TiO_2 and (0.5%)RGO/(50%)ZCS–TiO_2, respectively.

2.3. Characterization

Powder X-ray diffraction (PXRD) patterns were obtained using a Bruker D8 Advance X-ray diffractometer with Cu Kα radiation generated at 40 kV and 40 mA. Raman spectra were collected at room temperature on an inVia Reflex Micro-Raman Spectroscopy System (Renishaw Co.) with a 532 nm excitation source. Scanning electron microscopy (SEM, Hitachi New Generation SU8010) and transmission electron microscopy (JEM-2010, FEI, Tecnai G2 F20 FEG) were used to characterize the micromorphologies of the samples. UV-vis diffuse reflectance spectra were recorded on a Cary 500 UV-vis-NIR spectrophotometer with $BaSO_4$ as the background. X-ray photoelectron spectroscopy (XPS) measurements were carried out using a PHI Quantum 2000 XPS system with a monochromatic Al Kα source. The Brunauer–Emmett–Teller (BET) specific surface areas of the samples were measured with an ASAP2020M instrument. Photoluminescence (PL) spectra were obtained at room temperature on an Edinburgh FLS980 fluorescence spectrophotometer using a 365 nm excitation light source.

The photoelectrochemical measurements were carried out in a three-electrode system having an Ag/AgCl electrode and a Pt wire as the reference and counter electrodes, respectively. The photocurrent was measured *via* a BAS Epsilon workstation with a 300 W Xe lamp (PLS-SXE 300C, Beijing Perfectlight) equipped with a 420 nm cut-off filter as the visible light source. The electrochemical impedance spectra (EIS) were recorded using an electrochemical analyzer (Zahner, Germany).

2.4. Photoactivity tests

The photocatalytic H_2 production experiments were carried out in a Pyrex reaction cell with a closed gas circulation and evacuation system. A 300 W xenon lamp (PLS-SXE300C, Perfectlight Co., Beijing) equipped with a cut-off filter ($\lambda \geq 420$ nm) was used as the visible light source. In a typical photocatalytic test, 20 mg of the photocatalyst was mixed with 80 mL aqueous solution containing 0.35 M Na_2S and 0.25 M Na_2SO_3. The amount of evolved H_2 was quantitatively analyzed *via* online gas chromatography (GC).

3. Results and discussion

(X)ZCS–TiO_2 and (X)RGO/ZCS–TiO_2 composites were prepared through a solvothermal process, and we subsequently collected PXRD patterns of the materials to identify the crystalline phases. As shown in Fig. 1, the reflections corresponding to the TiO_2 nanofibers can be fully indexed to the standard peaks of anatase TiO_2 (JCPDS, No. 21-1272).[35] The diffraction peaks of ZCS are slightly shifted in comparison with those of ZnS (JCPDS, No. 77-2100) and CdS (JCPDS, No. 41-1049), which is consistent with the results of previous works and indicates the formation of a solid solution.[36,37] Moreover, the PXRD patterns of the ZCS–TiO_2 composites are matched well with those of anatase TiO_2 and ZCS, indicating that the crystal structure of the TiO_2 nanofibers is well maintained, and that ZCS was successfully loaded on the TiO_2 nanofiber surface (Fig. S1a, ESI†). However, no distinctive diffraction peaks corresponding to RGO were observed in the PXRD patterns of the RGO/ZCS–TiO_2 composites (Fig. S1b, ESI†), possibly because of its low loading and poor crystallinity.[23,38] Raman spectroscopy is a powerful tool for the analysis of carbon-containing systems such as graphene, so Raman spectra of the samples were obtained. As shown in Fig. S2 (ESI†), two characteristic peaks for the D (disordered) and G (graphitic) bands at 1345 and 1587 cm^{-1}, respectively, are visible in the spectra of the GO and 0.5%RGO/50%ZCS–TiO_2 samples. The ratio of intensities of the D and G bands (I_D/I_G) is a measure of the degree of disorder of a graphitic system, and this value for the RGO/ZCS–TiO_2 (1.02) composite was larger than that for pristine GO (0.96), indicating that the GO was partially reduced during the solvothermal process. These results indicate the presence of RGO in the RGO/ZCS–TiO_2 composites.

Fig. 1

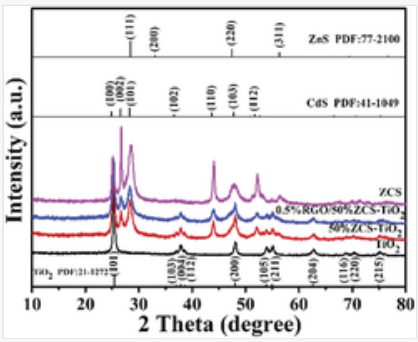

XRD patterns of TiO_2, ZCS, 50%ZCS–TiO_2, and 0.5%RGO/50%ZCS–TiO_2 composites.

Next, SEM and TEM images were obtained to observe the micro-morphologies of the as-prepared samples. As shown in Fig. 2a, the TiO_2 nanofibers have a typical cable-like morphology, and each fiber has a diameter of about 150 nm and a length of several micrometers. In contrast, the pure ZCS nanoparticles are spherical-like nanoparticles having an average size of about 300 nm (Fig. 2b). However, as a result of the unique one-dimensional morphology of the TiO_2 nanofibers, the agglomeration of ZCS nanoparticles was significantly reduced in the nanofiber-containing samples. In particular, small ZCS nanoparticles (between 5 and 20 nm in size) can be seen uniformly anchored on the TiO_2 nanofiber surface, even up to ZCS contents of 70% (Fig. S3a–d, ESI†), as shown in the TEM image (Fig. 2c), implying the formation of a heterostructure interface. The (HR)TEM image of 50%ZCS–TiO_2 (Fig. 2d) reveals the contact interface of ZCS and TiO_2. The lattice planes are visible, and the d-spacings of 0.35 and 0.31 nm can be assigned to the (101) planes of anatase TiO_2 and (101) planes of ZCS, respectively, which is consistent with the PXRD results, further demonstrating the successful synthesis of the ZCS–TiO_2 heterostructure composites. This close interfacial contact can facilitate interfacial charge transfer between ZCS and TiO_2. In addition, energy dispersive X-ray (EDX) analysis (Fig. S4, ESI†) revealed the presence of Ti, O, Zn, Cd, S, and C in the samples.

Fig. 2

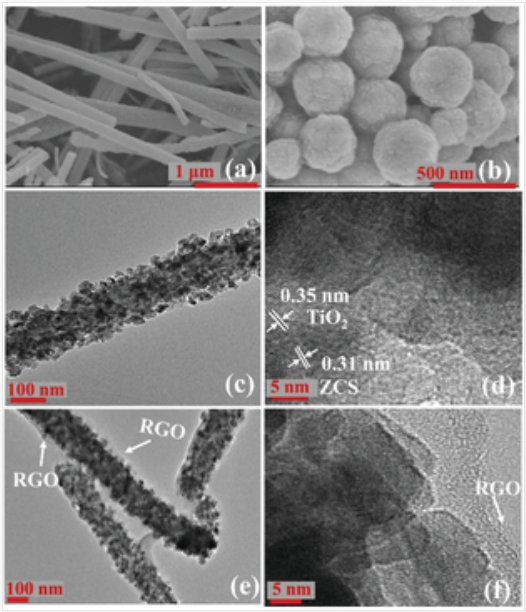

SEM images of (a) TiO_2 nanofibers, (b) ZCS, (c and d) TEM and HRTEM images of 50%ZCS–TiO_2, (e and f) TEM and HRTEM images of 0.5%RGO/50%ZCS–TiO_2.

Meanwhile, the N_2 adsorption–desorption isotherms were measured. As shown in Fig. S5 and Table S1 (ESI†), the BET surface areas of the ZCS–TiO_2 composites (32.10–38.04 m^2 g^{-1}) are significantly greater than that of pure ZCS (7.61 m^2 g^{-1}), which should result in the exposure of more active sites, and thus greater photocatalytic activity. Moreover, as expected, the introduction of RGO did not affect the morphology of the ZCS–TiO_2 composites (Fig. 2e). We also noted that ZCS–TiO_2 was tightly wrapped with ultrathin RGO nanosheets (Fig. 2e and f). According to previous reports, a close contact between ZCS–TiO_2 and RGO facilitates the transfer of photogenerated electrons, thus improving the separation efficiency of the photogenerated electron–hole pairs, and enhancing the photocatalytic performance.

Afterward, the UV-visible diffuse reflectance spectra of pure TiO_2, pure ZCS, and ZCS–TiO_2, as well as the RGO wrapped ZCS–TiO_2 composites, were used to evaluate their light absorption ability, which is crucial for determining their photocatalytic performance. It is clearly exhibited in Fig. 3a that pure TiO_2 absorbs UV light, and pure ZCS absorbs both UV and visible light. The band gaps of TiO_2 and ZCS were 3.22 eV and 2.44 eV (Fig. S6, ESI†), respectively, as calculated from the intercept of the tangents in the plot of the Kubelka–Munk function *versus* photon energy ($h\nu$).[39] The band gaps of the samples are listed in Table S2 (ESI†). Although the ZCS–TiO_2 composites have a similar light absorption range to ZCS, the absorption intensity is much reduced, but, as the ZCS content increased, the light absorption intensity gradually increased. Meanwhile, the absorption band edges of the ZCS–TiO_2 composites are blue-shifted compared to that of ZCS, possibly as a result of quantum confinement effects in the small ZCS nanoparticles in the ZCS–TiO_2 composites (see SEM images in Fig. S3, ESI† and TEM images in Fig. 2).[40] In addition, we also found (Fig. 3b) that the addition of RGO affects the absorption band edges of the ZCS–TiO_2 composites and enhances their visible light absorption, which may be beneficial for improving their photocatalytic performance.

Fig. 3

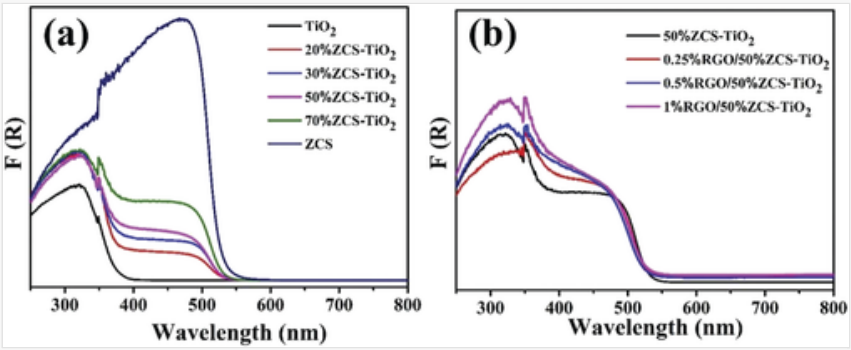

UV-vis diffuse reflectance spectra of (a) TiO_2, ZCS, and ZCS–TiO_2 composites with different weight ratios of ZCS, ~~and~~ (b) RGO/ZCS–TiO_2 composites with different weight ratios of RGO.

Furthermore, XPS measurements were used to analyze the chemical compositions and electronic states of the as-prepared samples. As shown in Fig. 4a, the Ti 2p spectrum displays two strong peaks at 458.7 and 464.4 eV, corresponding to Ti $2p_{3/2}$ and Ti $2p_{1/2}$ of TiO_2, respectively. Notably, the Ti 2p binding energies for ZCS–TiO_2 are lower than those of pure TiO_2, suggesting that electrons are transferred from TiO_2 to ZCS at the interface. In the pure ZCS sample, the peaks at 1045.6 and 1022.6 eV in the Zn 2p spectrum (Fig. 4b) can be assigned to the Zn $2p_{1/2}$ and Zn $2p_{3/2}$ electronic configurations of the +2 oxidation state, respectively. In addition, the peaks at 411.5 and 404.8 eV (Fig. 4c) in Cd 2p spectra correspond to the presence of Cd^{2+}. In comparison with those of pure ZCS, the Zn 2p binding energies for ZCS–TiO_2 are shifted to lower energies, whereas the Cd^{2+} 3d peaks are shifted to higher binding energies, suggesting that ZCS formed a strong interaction with the TiO_2 nanofibers. Thus, the XPS results suggest that an intimate heterojunction was formed between TiO_2 and ZCS. In addition, the XPS results also indicate that, after the introduction of RGO, a large number of oxygen-containing functional groups were added (Fig. S7, ESI†). However, the peak intensities related to oxygen-containing functional groups on the surface of 0.5%RGO/50%ZCS–TiO_2 were significantly reduced compared to those of GO, suggesting that the GO was effectively reduced to RGO by the solvothermal reduction.

Fig. 4

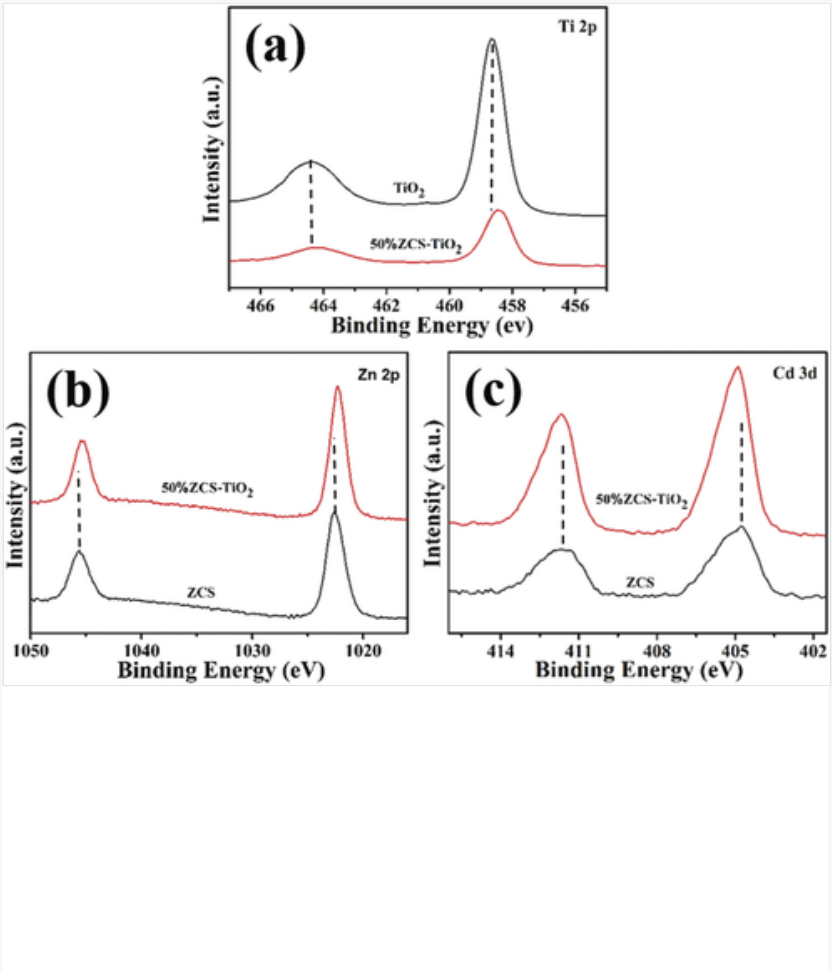

Comparisons of Ti 2p (a) XPS spectra of TiO_2 and 50%ZCS–TiO_2, comparisons of Zn 2p and Cd 3d (c) XPS spectra of ZCS and 50%ZCS–TiO_2.

The photocatalytic H_2 evolution activities of the as-prepared samples were evaluated in a Pyrex reaction cell under visible light irradiation, in which Na_2S and Na_2SO_3 were used as the sacrificial agents, and pure ZCS was used as a reference sample. No H_2 evolution was detected in the absence of light or photocatalysts. As shown in Fig. 5a, a negligible photocatalytic activity is observed in the presence of TiO_2 and Pt/TiO_2. Pure ZCS exhibited poor photocatalytic activity, yielding an H_2 evolution rate of merely 74.4 μmol h^{-1}, whereas the ZCS–TiO_2 composites showed much improved photocatalytic activities. In particular, 50%ZCS–TiO_2 yielded an H_2 production rate of 170.3 μmol h^{-1}, which is about 2.3 times higher than that of pure ZCS. However, the performance of an equivalent mechanically mixed sample (denoted as 50%ZCS + TiO_2) was significantly worse than that of the solvothermally prepared sample (*i.e.*, 50%ZCS–TiO_2). The poor photocatalytic activity of pure ZCS is mainly attributed to the fast recombination of the photogenerated electrons and holes and a limited number of exposed active sites. Therefore, the high dispersion of ultra-small ZCS nanoparticles tightly affixed to the TiO_2 nanofibers could not only significantly increase the number of exposed active sites but also accelerate the separation of the photogenerated carriers by forming a heterojunction between ZCS and TiO_2, thereby boosting the photocatalytic activity.

Moreover, it has been reported that RGO/graphene is ~~an excellent~~a good electron shuttle for photogenerated electrons, as well as an excellent metal-free cocatalyst for photocatalytic reactions. Therefore, the decoration of the catalyst surface with RGO may be the reason for the improvement in the photocatalytic activity of the ZCS–TiO_2 composites. Indeed, taking 50%ZCS–TiO_2 as an example, the addition of a small amount of RGO (0.5 wt%) enhanced the H_2 production rate to 299.0 μmol h^{-1} (Fig. 5b), approximately 1.8 times higher than that of the pristine catalyst, 2.9 times higher than that of 0.5 wt%RGO/ZCS, and 1.4 times higher than that of the 50%ZCS–TiO_2 catalyst loaded with 0.5 wt% Pt (0.5 wt%Pt/50%ZCS–TiO_2) (Fig. S8, ESI†). However, the addition of excess RGO has a negative effect on the photocatalytic activity, possibly hindering light absorption by the ZCS–TiO_2 composite.[41,42] The apparent quantum efficiency (AQE) of 0.5%RGO/50%ZCS–TiO_2 is 11.9% at 420 nm. The photocatalytic performance of the 0.25%RGO/0.5%Pt(50%)ZCS–TiO_2 sample was 1.8 fold higher than that of the 0.25%RGO/50%ZCS–TiO_2 sample (Fig. S9, ESI†), which could be attributed to the introduction of Pt as a cocatalyst, which effectively improved the

photocatalytic activity. For the 0.5%RGO/0.5%Pt(50%)ZCS–TiO_2 and 1%RGO/0.5%Pt(50%)ZCS–TiO_2 samples, the activity was almost unchanged. High concentrations of RGO can effectively promote the transfer of photogenerated electrons, leading to excellent activity, nullifying the role of Pt as a cocatalyst. Therefore, we can conclude that GO serves as an excellent cocatalyst in this system. Table S3 (ESI†) shows the comparative photocatalytic H_2 evolution over CdS-based and RGO-based photocatalysts, which indicates the excellent activity of the RGO/ZCS–TiO_2 nanocomposites.

Fig. 5

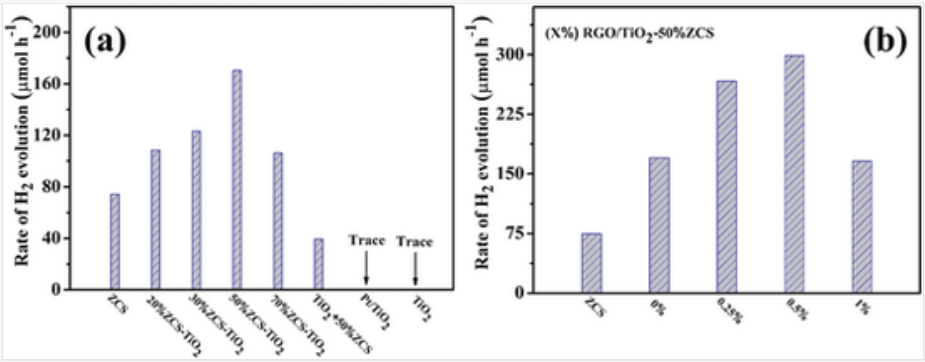

(a) Photocatalytic H_2 evolution rate over ZCS, TiO_2, Pt/TiO_2, a mechanical mixture of TiO_2 and ZCS, ZCS–TiO_2 composites with different weight ratios of ZCS, (b) photocatalytic H_2 evolution rate over ZCS and RGO/50%ZCS–TiO_2 composites with different weight ratios of RGO. (Reaction conditions: 80 mL H_2O containing 0.35 M Na_2S and 0.25 M Na_2SO_3; visible light ($\lambda \geq 420$ nm); catalyst: 20 mg.)

In addition, the photocatalytic stability of the RGO-decorated ZCS–TiO_2 composite (0.5%RGO/50%ZCS–TiO_2) was further investigated using recycling tests. As shown in Fig. 6a, the H_2 evolution rate of the composite did not deteriorate over four reuse cycles, indicating its stability. Meanwhile, the PXRD patterns (Fig. 6b) of the composite remained similar to that of the original sample after the recycling tests, further demonstrating that the RGO/ZCS–TiO_2 composites are stable and recyclable photocatalysts. In addition, SEM observations (Fig. S10a and b, ESI†) and XPS measurements (Fig. S10c–e, ESI†) revealed no significant changes in the morphology and surface chemical states of the sample before and after the catalytic reaction. The abovementioned results demonstrate that the RGO/ZCS–TiO_2 composites show excellent reusability and stability during the catalytic reaction.

Fig. 6

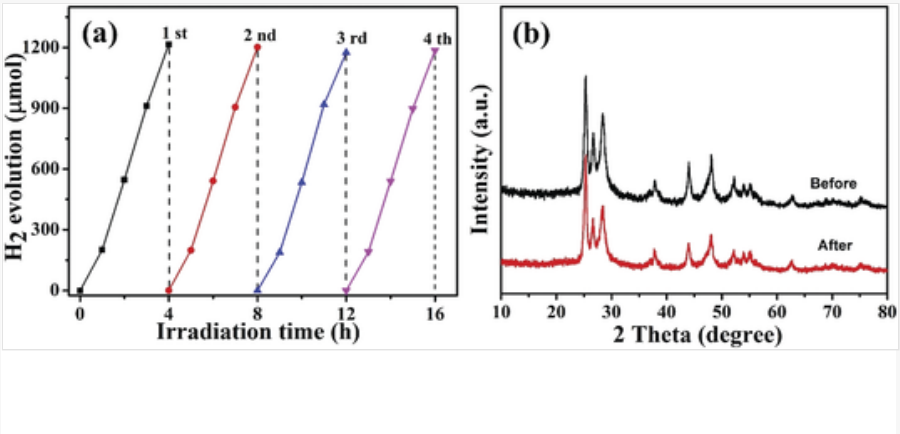

(a) Cycle runs for the photocatalytic H_2 production of 0.5%RGO/50%ZCS–TiO_2, and (b) XRD patterns of 0.5%RGO/50%ZCS–TiO_2 before and after the photocatalytic reaction.

We also carried out electrochemical measurements to identify the origin of the enhanced photocatalytic performance of the RGO/ZCS–TiO_2 composites. Fig. 7a shows the photocurrent spectra of different samples under visible light irradiation. The photocurrent of 50%ZCS–TiO_2 is much greater than those of pure ZCS, TiO_2, and 50%ZCS + TiO_2, indicating that the high dispersion of ultra-small ZCS particles on the TiO_2 surface improves the separation of

photogenerated carriers. As expected, the decoration of the catalyst surface with RGO can significantly increase the photocurrent, further indicating the accelerated transfer photogenerated electrons, thus improving the separation efficiency of the photogenerated electron–hole pairs. Moreover, EIS measurements were used to understand the charge transfer kinetics. As shown by the Nyquist plots in Fig. 7b, 0.5%RGO/50%ZCS–TiO_2 has a much smaller semicircle diameter than those of 50%ZCS–TiO_2, TiO_2, 50%ZCS + TiO_2 and ZCS, further demonstrating that the high dispersion of ultra-small ZCS particles on the TiO_2 nanofiber surface and the introduction of RGO effectively promote the transfer of photogenerated electrons and lead to enhanced photocatalytic activity.

Fig. 7

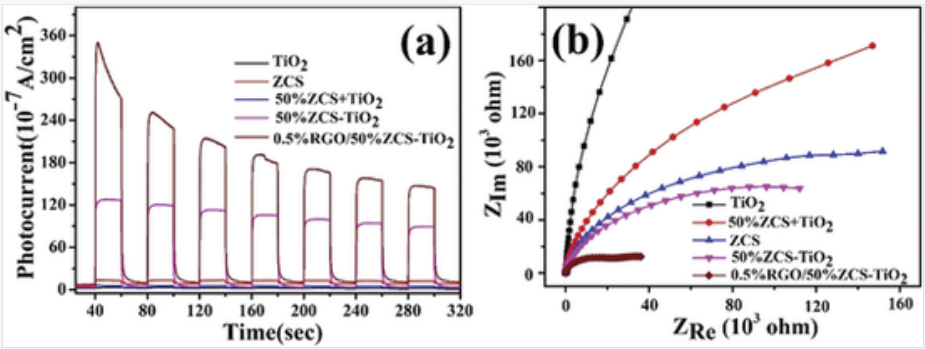

(a) Transient photocurrent response and (b) Nyquist impedance plots of TiO_2, ZCS, 50%ZCS + TiO_2, 50%ZCS–TiO_2 and 0.5%RGO/50%ZCS–TiO_2.

PL spectra are useful to reveal the charge transfer and charge-carrier separation behavior of photocatalysts. As shown in Fig. S11 (ESI†), the PL intensity of 50%ZCS–TiO_2 is much lower than those of ZCS and 50%ZCS + TiO_2, implying significantly less electron–hole recombination. The enhanced charge separation in 50%ZCS–TiO_2 can be ascribed to the formation of a heterojunction between ZCS and TiO_2. After RGO was introduced into the 50%ZCS–TiO_2 system, the PL intensity reached the lowest value with respect to the ZCS, 50%ZCS + TiO_2 and 50%ZCS–TiO_2 systems, indicating that this sample has the highest photogenerated charge separation efficiency, which is likely the reason for the superior photocatalytic H_2 evolution activity; that is, the fast interfacial electron transfer from the light-trapping centers in ZCS to RGO through TiO_2. Furthermore, the PL spectra analyses are also consistent with the photocurrent and EIS results.

To identify the active species during hydrogen production, some sacrificial agents were used to capture active species. Fig. S12 (ESI†) shows the radical trapping experiments of 0.5%RGO/50%ZCS–TiO_2, with the addition of *tert*-butyl alcohol (TBA) to trap hydroxyl radicals ($^{\cdot}OH$) and CCl_4 to trap e^-.[43,44] The photocatalytic performance of 0.5%RGO/50%ZCS–TiO_2 reveals a drastic reduction in activity (~40%) after the addition of CCl_4, which shows that e^- electrons are the active species involved in the photocatalytic H_2 production. In contrast, the photocatalytic H_2 production activity is hardly affected by the addition of TBA (~12%). Hence, the active species contributing to the photocatalytic H_2 activity of the samples are e^-.

Using the band gap energy (E_g) of ZCS (2.44 eV) and the formulae $E_{CB} = \chi - 0.5E_g - E_C$ and $E_{VB} = \chi + 0.5E_g - E_C$ (*vs.* NHE),[~~6,45~~45] where χ, E_g, E_{CB}, E_{VB}, and E_C are the absolute electronegativity of the composite and the energies of the band gap, conduction band, valence band, and free electrons, respectively, and $\chi = 5.35$ eV and $E^C = 4.5$ eV, we calculated $E_{CB} = -0.37$ eV *vs.* NHE (pH = 0). Based on all of the results and the calculations above, a possible reaction mechanism for photocatalytic H_2 evolution over the RGO/ZCS–TiO_2 composites is proposed. As shown in Fig. 8, under visible light irradiation, ZCS is excited to generate photogenerated electron–hole pairs. The photogenerated electrons in the conduction band of ZCS can migrate to TiO_2 to promote the effective separation and transfer of photogenerated electron–hole pairs. When RGO is introduced, it promotes the separation of photogenerated carriers and extends their lifetimes. In addition, RGO not only promotes electron transport but acts as a non-noble metal H_2 production cocatalyst. Therefore, the photogenerated electrons that migrate to TiO_2 can further move to RGO, and RGO suppresses the recombination of the charge carriers and increases the photocatalytic H_2 evolution activity of RGO/ZCS–TiO_2.

Fig. 8

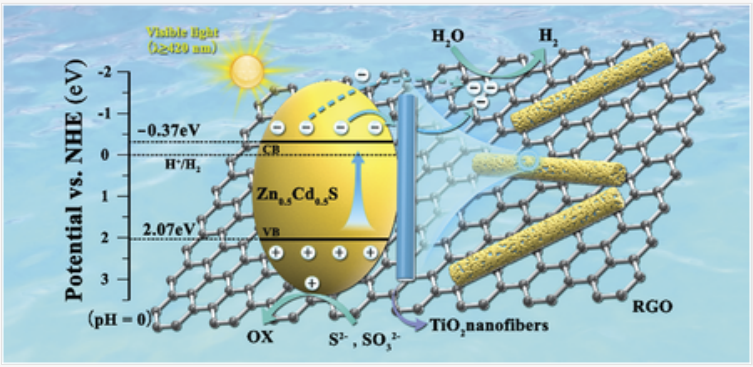

Schematic illustration of the possible charge transfer and separation in the RGO/ZCS–TiO_2 system under visible light illumination.

4. Conclusions

In summary, ZCS–TiO_2 heterojunction photocatalysts and composites with RGO were prepared using a facile solvothermal strategy. The ZCS–TiO_2 heterojunction photocatalysts containing 50% ZCS (0.5%RGO/50%ZCS–TiO_2) showed the optimal performance for photocatalytic H_2 evolution: 2.3 and 4.3 times higher than those of ZCS alone and mechanically mixed samples, respectively. The superior photocatalytic performance of ZCS–TiO_2 is due to the formation of a heterojunction, which results in efficient charge transfer and separation. When RGO was introduced as a cocatalyst, the 0.5%RGO/50%ZCS–TiO_2 composites exhibited the best performance for photocatalytic H_2 evolution, 1.8 and 4.0 times better than those of 50%ZCS–TiO_2 and ZCS, respectively. Thus, the introduction of TiO_2 and RGO led to the formation of many electron transfer and transport paths, which effectively promoted the rapid separation and migration of photogenerated electron–hole pairs in the photocatalytically active ZCS component and further extended the lifetimes of the photogenerated charge carriers. Therefore, this study demonstrates the great potential of modified ZCS-based materials as photocatalysts for the photocatalytic H_2 evolution from water.

Conflicts of interest

There are no conflicts to declare.

Acknowledgements

This work was supported by the National Natural Science Foundation of China (No. 21872032 and 21273036), the Key Scientific and Technological Project of Henan Province (No. 202102210054), the independent innovation application research project (No. K2020YY001) and the Young Backbone Teacher of Zhongyuan University of Technology.

References can be edited in the panel that appears to the right when you click on a reference.

1 X. Chen, S. Shen, L. Guo and S. S. Mao, *Chem. Rev.*, 2010, **110**, 6503–6570.

2 S. Chandrasekaran, L. Yao, L. Deng, C. Bowen, Y. Zhang, S. Chen, Z. Lin, F. Peng and P. Zhang, *Chem. Soc. Rev.*, 2019, **48**, 4178–4280.

3 Z. Gao, K. Chen, L. Wang, B. Bai, H. Liu and Q. Wang, *Appl. Catal., B*, 2020, **268**, 118462.

4 A. Kumar and V. Krishnan, *Adv. Funct. Mater.*, 2021, **31**, 2009807.

5 A. Kumar, A. Kumar and V. Krishnan, *ACS Catal.*, 2020, **10**, 10253–10315.

6 Z. Jin, T. Wei, F. Li, Q. Zhang and L. Xu, *New J. Chem.*, 2020, **44**, 3471–3477.

7 H.-B. Huang, Z.-B. Fang, K. Yu, J. Lü and R. Cao, *J. Mater. Chem. A*, 2020, **8**, 3882–3891.

8 X. J. Zhou, H. Yu, D. Zhao, X. C. Wang and S. T. Zheng, *Appl. Catal., B*, 2019, **248**, 423–429.

9 H. She, Y. Sun, S. Li, J. Huang, L. Wang, G. Zhu and Q. Wang, *Appl. Catal., B*, 2019, **245**, 439–447.

10 T. Yu, Z. Lv, K. Wang, K. Sun, X. Liu, G. Wang, L. Jiang and G. Xie, *J. Power Sources*, 2019, **438**, 227014.

11 Y. Zhang, Y.-Z. Lin, Z.-X. Wang, K. Li, T. Li and F.-T. Liu, *Catal. Sci. Technol.*, 2019, **9**, 583–587.

12 M. Ahmad, X. Quan, S. Chen, H. Yu and Z. Zeng, *Appl. Catal., B*, 2021, **283**, 119601.

13 Y. Xia, P. Yang, Y. Sun, Y. Wu, B. Mayers, B. Gates, Y. Yin, F. Kim and H. Yan, *Adv. Mater.*, 2003, **15**, 353–389.

14 L. Zhang, J. C. Yu, M. Mo, L. Wu, K. W. Kwong and Q. Li, *Small*, 2005, **1**, 349–354.

15 H. Li, Q. Zhou, Y. Gao, X. Gui, L. Yang, M. Du, E. Shi, J. Shi, A. Cao and Y. Fang, *Nano Res.*, 2015, **8**, 900–906.

16 E. N. Alvar, B. Zhou and S. H. Eichhorn, *J. Mater. Chem. A*, 2016, **4**, 6540–6552.

17 X. Zhang, X. Li, C. Shao, J. Li, M. Zhang, P. Zhang, K. Wang, N. Lu and Y. Liu, *J. Hazard. Mater.*, 2013, **260**, 892–900.

18 T. Cao, Y. Li, C. Wang, C. Shao and Y. Liu, *Langmuir*, 2011, **27**, 2946–2952.

19 C. J. Luo, S. D. Stoyanov, E. Stride, E. Pelan and M. Edirisinghe, *Chem. Soc. Rev.*, 2012, **41**, 4708–4735.

20 L. Hu, J. Yan, C. Wang, B. Chai and J. Li, *Chin. J. Catal.*, 2019, **40**, 458–469.

21 M. Kim, Y. K. Kim, S. K. Lim, S. Kim and S.-I. In, *Appl. Catal., B*, 2015, **166**–**167**, 423–431.

22 K. Zhang, Y. Dai, Z. Zhou, S. U. Jan, L. Guo and J. R. Gong, *Nano Energy*, 2017, **41**, 101–108.

23 C. Xue, H. Li, H. An, B. Yang, J. Wei and G. Yang, *ACS Catal.*, 2018, **8**, 1532–1545.

24 K. Chang, X. Hai and J. Ye, *Adv. Energy Mater.*, 2016, **6**, 1502555.

25 S. Kumar, N. L. Reddy, H. S. Kushwaha, A. Kumar, M. V. Shankar, K. Bhattacharyya, A. Halder and V. Krishnan, *ChemSusChem*, 2017, **10**, 3588–3603.

26 A. Meng, L. Zhang, B. Cheng and J. Yu, *ACS Appl. Mater. Interfaces*, 2019, **11**, 5581–5589.

27 K. I. Bolotin, K. J. Sikes, Z. Jiang, M. Klima, G. Fudenberg, J. Hone, P. Kim and H. L. Stormer, *Solid State Commun.*, 2008, **146**, 351–355.

28 M. D. Stoller, S. Park, Y. Zhu, J. An and R. S. Ruoff, *Nano Lett.*, 2008, **8**, 3498–3502.

29 F. He, A. Meng, B. Cheng, W. Ho and J. Yu, *Chin. J. Catal.*, 2020, **41**, 9–20.

30 Y.-J. Cho, H. Kim, S. Lee and W. Choi, *J. Catal.*, 2015, **330**, 387–395.

31 Y. Chen, H. Ge, L. Wei, Z. Li, R. Yuan, P. Liu and X. Fu, *Catal. Sci. Technol.*, 2013, **3**, 1712–1717.

32 K. Manjunath, V. S. Souza, G. Nagaraju, J. M. L. Santos, J. Dupont and T. Ramakrishnappa, *New J. Chem.*, 2016, **40**, 10172–10180.

33 A. Kumar, V. Navakoteswara Rao, A. Kumar, A. Mushtaq, L. Sharma, A. Halder, S. K. Pal, M. V. Shankar and V. Krishnan, *ACS Appl. Energy Mater.*, 2020, **3**, 12134–12147.

34 N. Qin, J. Xiong, R. Liang, Y. Liu, S. Zhang, Y. Li, Z. Li and L. Wu, *Appl. Catal., B*, 2017, **202**, 374–380.

35 X. Pan and Y.-J. Xu, *J. Phys. Chem. C*, 2015, **119**, 7184–7194.

36 J. Ran, J. Zhang, J. Yu and S. Z. Qiao, *ChemSusChem*, 2014, **7**, 3426–3434.

37 X. Zhou, N. Zhang, L. Yin, Y. Zhao and B. Zhang, *Ceram. Int.*, 2020, **46**, 26100–26108.

38 J. Zhang, J. Yu, M. Jaroniec and J. R. Gong, *Nano Lett.*, 2012, **12**, 4584–4589.

39 P. Jin, L. Wang, X. Ma, R. Lian, J. Huang, H. She, M. Zhang and Q. Wang, *Appl. Catal., B*, 2021, **284**, 119762.

40 X. Zong, Z. Xing, H. Yu, Y. Bai, G. Q. M. Lu and L. Wang, *J. Catal.*, 2014, **310**, 51–56.

41 L. Ye, J. Fu, Z. Xu, R. Yuan and Z. Li, *ACS Appl. Mater. Interfaces*, 2014, **6**, 3483–3490.

42 S. Liu, Z. Chen, N. Zhang, Z.-R. Tang and Y.-J. Xu, *J. Phys. Chem. C*, 2013, **117**, 8251–8261.

43 H. Tian, M. Liu and W. Zheng, *Appl. Catal., B*, 2018, **225**, 468–476.

44 H. Tian, K. Shen, X. Hu, L. Qiao and W. Zheng, *J. Alloys Compd.*, 2017, **691**, 369–377.

45 J. Song, H. Zhao, R. Sun, X. Li and D. Sun, *Energy Environ. Sci.*, 2017, **10**, 225–235.

Footnotes

[†] Electronic supplementary information (ESI) available. See DOI: 10.1039/d1nj04195a

Queries and Answers

Q1

Query: For your information: You can cite this article before you receive notification of the page numbers by using the following format: (authors), New J. Chem., (year), DOI: 10.1039/d1nj04195a.

Answer: Ok. Thank you.

Q2

Query: Have all of the author names been spelled and formatted correctly? Names will be indexed and cited as shown on the proof, so these must be correct. No late corrections can be made.

Answer: Yes

Q3

Query: Have all of the funders of your work been fully and accurately acknowledged?

Answer: Yes